

See discussions, stats, and author profiles for this publication at: <https://www.researchgate.net/publication/51575551>

Evolution of Ordering in Iron Oxide Nanoparticle Monolayers Using Electrophoretic Deposition

ARTICLE *in* ACS APPLIED MATERIALS & INTERFACES · AUGUST 2011

Impact Factor: 6.72 · DOI: 10.1021/am200830f · Source: PubMed

CITATIONS

15

READS

20

3 AUTHORS:



Alexander James Krejci

State University of New York, Korea

23 PUBLICATIONS 155 CITATIONS

SEE PROFILE



Isabel Gonzalo

Technical University Darmstadt

20 PUBLICATIONS 153 CITATIONS

SEE PROFILE



James H. Dickerson

Brookhaven National Laboratory

117 PUBLICATIONS 824 CITATIONS

SEE PROFILE

Evolution of Ordering in Iron Oxide Nanoparticle Monolayers Using Electrophoretic Deposition

Alex J. Krejci,^{†,‡} Isabel Gonzalo-Juan,^{†,‡} and James H. Dickerson^{†,‡,*}

[†]Department of Physics and Astronomy, Vanderbilt University, Nashville, Tennessee 37235-1807, United States

[‡]Vanderbilt Institute of Nanoscale Science and Engineering, Vanderbilt University, Nashville, Tennessee 37234-0106, United States

S Supporting Information

ABSTRACT: Iron-oxide nanoparticle monolayers and multilayers were assembled using dc electrophoretic deposition. The rate of deposition and the total particle deposition were controlled by varying the concentration of nanoparticles and the deposition time, respectively. Using scanning electron microscopy, we performed a time-resolved study that demonstrated the growth of the monolayer from a single isolated nanoparticle to a nearly complete layer. We observed tight, hexagonal packing of the nanoparticles indicating strong particle–particle interaction. Multilayer growth was assessed using scanning electron microscopy and atomic force microscopy, revealing a monolayer-by-monolayer growth process.

KEYWORDS: iron oxide, monolayer, electrophoretic deposition, nanocrystal, thin film, wüstite, spinel

Studies of nanoparticle (NP) monolayer formation have been motivated by potential applications of the films in magnetic storage, surface-enhanced Raman scattering (SERS) coatings, biosensors.^{1–4} Potential applications of NP monolayers rely on fabrication techniques that are facile, rapid, and site selective. Three of the most common techniques used to create monolayer films are Langmuir–Blodgett, ligand-mediated self-assembly, and evaporative self-assembly.^{5–14} In this article, we demonstrate monolayer formation using an alternative technique, electrophoretic deposition (EPD). EPD is a rapid, scalable technique often used for the fabrication of homogeneous and dense thin films.^{15–25} EPD using ac fields has frequently been employed to create monolayers.^{26,27} In ac-EPD, electrohydrodynamic flow of the solvent, in which the NPs are dispersed, causes lateral motion of NPs. The lateral motion of the NPs facilitates monolayer assembly in ac depositions. In contrast, we have created monolayer films through EPD with dc electric fields. To the best of our knowledge, this is the first observation of ordered, nanosphere monolayer formation using EPD in nonmetallic systems.²⁸ In 1993, dc-EPD (hereafter, EPD) was used to form well-ordered monolayers of citrate-stabilized gold nanoparticles.²⁹ Then in 1997, platinum NP monolayers were formed through dc fields.³⁰ In our work, by controlling both the deposition rate and the total particle deposition, we present the step-by-step formation of an iron oxide NP monolayer and multilayer through EPD.

NP SYNTHESIS & CHARACTERIZATION

FeO/Fe₃O₄ core–shell NPs were synthesized using thermal decomposition³¹ of an iron oleate precursor in the presence of oleic acid. First, we synthesized the oleate precursor by mixing 2.17 g of FeCl₃ · 6H₂O (Sigma Aldrich) and 7.30 g of sodium oleate (Sigma Aldrich) with 16 mL of ethanol (Pharmco-AAPER) 28 mL of hexane (Fisher), and 12 mL of deionized water. We then heated the mixture to 70 °C and maintained this temperature for four hours. Next, we synthesized the NPs by thermal decomposition of a solution containing 1.6 mmol of iron

oleate and 0.8 mmol of oleic acid in 10 mL of 1-octadecene (Sigma Aldrich). We mixed the solution and degassed it at 100 °C for 30 min, whereupon we heated the solution at a rate of 3 °C/min to 320 °C. We finally refluxed the solution for 45 min.

The nanocrystals were characterized using a variety of diagnostic techniques prior to experiments. High-resolution transmission electron microscopy images (TEM) were collected on a Philips CM20 microscope operating at an accelerating voltage of 200 kV. TEM samples were prepared on a copper grid covered with ultrathin carbon type-A film (Ted Pella, Inc.). X-ray diffraction (XRD) measurements on powders of the NPs were obtained using a Scintag X₁ Θ/Θ powder X-ray diffractometer under irradiation from a Cu K_α source ($\lambda = 1.5406 \text{ \AA}$). The samples were cast onto a zero-background Si(511) substrate for the measurements. Absorption spectroscopy was conducted on a Varian Cary 5000 UV–vis–NIR spectrophotometer. Electrophoretic mobility and hydrodynamic diameter measurements of the NP suspensions were performed on a Malvern Zetasizer Nano ZS. The electrophoretically deposited films of NPs were characterized through scanning electron microscopy (SEM) on a Raith eLine as well as a JEOL JSM-6701 F operating at 5 kV and through atomic force microscopy (AFM) on an Agilent 5400 series atomic force microscope in tapping mode with NSC15 AFM tips with a probe radius of 10 nm.

EXPERIMENT & DISCUSSION

The XRD data, shown in Figure 1a, revealed FeO peaks (wüstite JCPDF #46–1312) and spinel phase iron oxide, comprised either of γ -Fe₂O₃ (maghemite JCPDF #39–1346) or of Fe₃O₄ (magnetite JCPDF #19–0629). Scherrer analysis of these peaks suggested a NP core diameter of $7 \pm 3 \text{ nm}$ and a shell thickness of $4 \pm 2 \text{ nm}$, resulting in a net NP diameter of

Received: June 27, 2011

Accepted: August 16, 2011

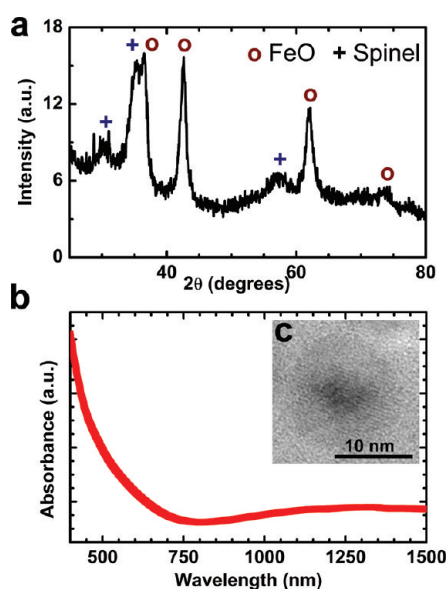


Figure 1. (a) XRD of NPs with wüstite and spinel phase peaks of iron oxide identified, corresponding to the core and shell of the NP, respectively. (b) Absorption curve confirmed the spinel phase is Fe_3O_4 . (c) TEM of our typical NP, showing the core–shell structure.

15 ± 7 nm. Since XRD cannot easily discern between $\gamma\text{-Fe}_2\text{O}_3$ or Fe_3O_4 , we performed complementary absorption spectroscopy measurements on the NPs. Fe_3O_4 possesses well-known absorption features in the IR that are not present in $\gamma\text{-Fe}_2\text{O}_3$. The strong absorption below ~ 640 nm and the moderate absorption in the IR region, peaking at ~ 1300 nm (Figure 1b), confirm that the shell layer of the NPs consists of Fe_3O_4 .³² TEM micrographs, shown in Figure 1c, revealed monodisperse core–shell NPs with a mean diameter of 16.5 ± 1.2 nm, and an error in fitting the mean of 0.1 nm. This value, within uncertainty, is comparable to the diameter as determined by XRD.

To perform the monolayer deposition, we first mounted two rectangular, epitaxial, doped Si wafers parallel to each other with a 5 mm wide gap between the two wafers (Figure 2). Each wafer was $1 \times 0.5 \text{ cm}^2$ in size. Using the wafers as electrodes, we applied a 500 V potential across the 5 mm gap. The electrodes were then slowly (duration ~ 20 s) inserted ~ 2.5 cm into a suspension of well-dispersed iron oxide NPs in hexane with a 1 mg/mL concentration. We partially extracted the electrodes by 3 mm four times during the deposition (~ 20 s, ~ 50 s, ~ 100 s, ~ 140 s) before extracting the electrodes completely after ~ 180 s. The 500 V potential remained on for 3 min after complete extraction to facilitate drying of the solvent.^{22,24,33,34} Thereafter, we turned off the voltage supply. This stepwise extraction resulted in a film containing five distinct regions that differ only by the amount of time said region remained in the NP solution. By imaging each region of the film using a SEM, we were able to observe film growth as a function of deposition time. Two types of NP films were created using the aforementioned technique, one which formed a nearly complete monolayer (monolayer film) and another which formed multiple layers (multilayer film). We controlled the total nanoparticle deposition by varying both the charged nanoparticle concentration and the deposition time. Charged nanoparticle concentration is controlled by depositing particles prior to depositing the films assessed below, and results in an immeasurable change in total concentration. Our discussion

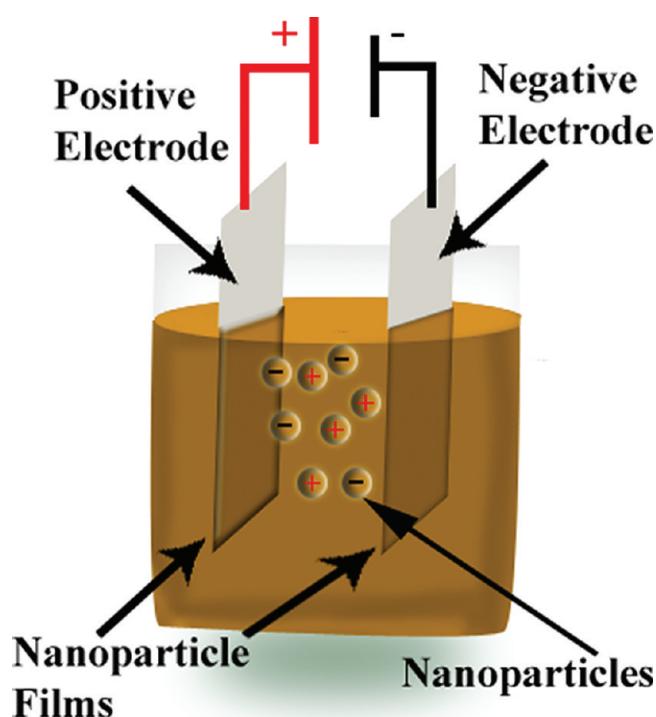


Figure 2. Schematic of electrophoretic deposition process. Two electrodes are mounted to form a parallel plate capacitor. A voltage was applied, and the electrodes were inserted into a solution of hexane and iron oxide NPs.

will first focus on the formation of NP monolayers, followed by NP multilayer films.

The chronology of the growth of a NP monolayer film is displayed in Figure 3. The figures depict representative regions of the film at three stages of the monolayer formation. Using these images, we have extracted information regarding the formation of the film, which allows for better understanding of EPD film formation. Figure 3a displays the region of the NP film after 20 s of deposition, the shortest deposition time in the experiment. As can be seen, many of the NPs arranged to form clusters; some particles deposited singly onto the electrode. These isolated particles confirmed that the NPs were well dispersed as monomers in suspension. Dynamic light scattering data on the EPD suspensions supported this conclusion; the average hydrodynamic diameter for the nanoparticles (Figure 4) was $17 \text{ nm} \pm 3 \text{ nm}$, comparable to the diameter determined from TEM. Based on this evidence, we assert that the NPs experienced uniform electrophoresis toward the electrodes. Despite this assertion, the particles did not exhibit a uniform, evenly dispersed deposition onto the substrate. From these observations, we conclude that the initially well-dispersed NPs must have experienced lateral, attractive interactions between each other during the electrophoretic process to form the observed clusters. These interactions may have occurred at the electrophoretic double layer near the surface of the electrode or on the surface of the electrode where the NPs possessed some lateral, two-dimensional physical mobility prior to irreversibly depositing.^{16,17,35}

Closer inspection of the clusters revealed that the nanoparticles formed a two-dimensional hexagonal packing arrangement. To verify this, we performed a Fourier transform (Figure 3a, bottom inset) on the magnified region of Figure 3a. The Fourier

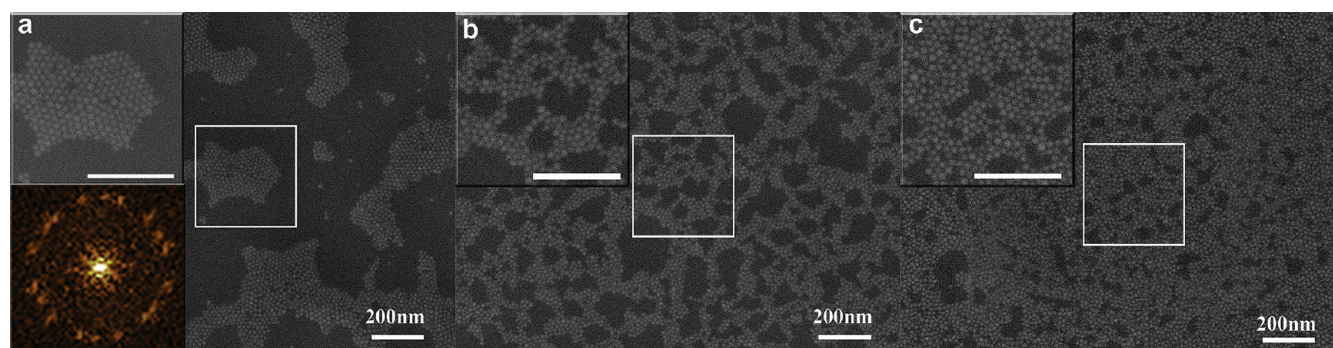


Figure 3. Chronological growth of a single monolayer. (a) After 20 s of deposition, clusters form into hexagonally packed domains. The upper inset shows a magnified section of the image, and the lower inset shows a Fourier transform of the upper inset—three hexagonally packed domains create the ring composed of 18 dots. (b) After 97 s, the film has grown into a network by merging of clusters. (c) After 180 s, particles deposit within voids of network to form a nearly complete monolayer; no three-dimensional growth is observed. (Inset scale bar, 200 nm; solution concentration, 1 mg/mL).

transform consists of an 18 point ring. A single hexagonally packed domain of nanoparticles should contain six points, evenly spaced around in a ring. Thus, the Fourier transform in Figure 3a indicated the presence of three domains of hexagonally packed particles. From this we assert that three initially independent clusters of NPs, each with different crystallographic orientations and, hence, comprised individual domains, have merged together.

Lastly, we noted how closely the nanoparticles were packed. A small visible gap existed between the nanoparticles within a hexagonally packed domain. We quantified the center–center spacing between the particles in the SEM micrographs by measuring the edge-to-edge distance of chains of NPs contained within a hexagonally packed domain. We only included in the data set chains at least six NPs long to minimize error associated with identifying the location of a particle's edge. The average center-to-center spacing between hexagonally packed particles, CtC , yielded a value of 17.3 ± 0.1 nm. This yielded an edge-to-edge spacing of 0.8 ± 0.1 nm (see the Supporting Information). Fourier transform data and particle spacing measurements indicate that particle–particle interactions gave rise to local (up to ~ 150 particles), tightly packed arrangements among the nanoparticles.

The next image, Figure 3b, depicts nanoparticle deposition after 97 s. We first noticed that a complete absence of isolated nanoparticles existed in the layer. As additional NPs reached the surface of the electrode, newly every deposited particle became incorporated into a cluster. Second, the individual clusters combined to form a continuous network of clusters. Clusters frequently appeared to connect by forming thin chains of NPs that link neighboring clusters. The network created by these chain structures may have been driven by electric field gradients emanating from and ambient to NPs in the monolayer.^{36–40} Such large field gradients emerging from a single NP at the end of a chain or at the vertex of a cluster of NPs can act as a focal point for the aggregation and subsequent deposition of nanoparticles in the monolayer. Therefore, the observed cluster network and chain growth likely arose from the large gradient fields emanating from the NPs in the nonpolar suspension environment.

Figure 3c is an image of the nanoparticle deposit after 180 s, the final region examined in the monolayer film. The majority of the large voids in the film were filled; only relatively small voids remained. Interestingly, the film formation remained two-dimensional during the completion of the formation of a monolayer. For this to occur, presuming isotropic deposition of the NPs from a uniform suspension (even if the absolute

concentration had changed from the initial concentration), NPs that normally would have deposited to create the second layer must have possessed sufficient lateral mobility to migrate toward the voids in the underlying monolayer, subsequently filling in the space, or must have dislodged other NPs from their positions to burrow into the extant, underlying monolayer. Gradient electric fields from isolated NPs and small NP clusters also may have drawn NPs into the monolayer, thus preserving the two-dimensional growth. Whatever the exact mechanism was, nanoparticles were driven to occupy voids in the monolayer before the beginning of the formation of the next layer, the bilayer.

The images of Figure 3 facilitated the assessment of the time dependence of the film formation, which can reveal information about the conditions of EPD. We measured the nanoparticle density of the film by counting the number of particles per area observed under SEM. For each time interval, a minimum of five images were selected for analysis from random sections of the film. The results (Figure 5) indicated a linear increase in nanoparticle density in the monolayer as a function of time. The slope of the line, $7.0 \times 10^6 \pm 2.0 \times 10^6$ particles/s mm², represents particle flux rate, whereas the intercept $1.2 \times 10^9 \pm 2.0 \times 10^8$ particles/mm², indicates the initial particle flux was much higher. Sarkar and Nicholson explored the time dependence of material deposition in EPD film formation using polar solvents, measuring the total deposited weight of the materials in a film rather than the particle density that we measured here.²⁰ In their work, they explored four possible EPD conditions—constant voltage/constant particle concentration, constant voltage/variable concentration, constant current/constant concentration, and constant current/variable concentration—that could give rise to notably different time dependences of the total deposited weight.²⁰ Our result is most consistent with deposition under constant voltage and constant concentration conditions.

A possible explanation for this lies with the mobility of the nanoparticles. We estimated the time it takes for a single positive particle to traverse the 5 mm gap (d) between the electrodes by employing the average value of the electrophoretic mobility ($\mu \equiv v/E$, Figure 4b) of the suspension and the voltage applied during EPD ($E = V/d$), assuming a parallel plate configuration with a spatially and temporally constant electric field. The result, ~ 30 s, suggests that the majority of the charged nanoparticles that initially existed within the gap between the electrodes had likely reached the electrode within this period. This is supported by

mobility measurements of the solution before and after EPD (see the Supporting Information). As no visible flocculation appeared

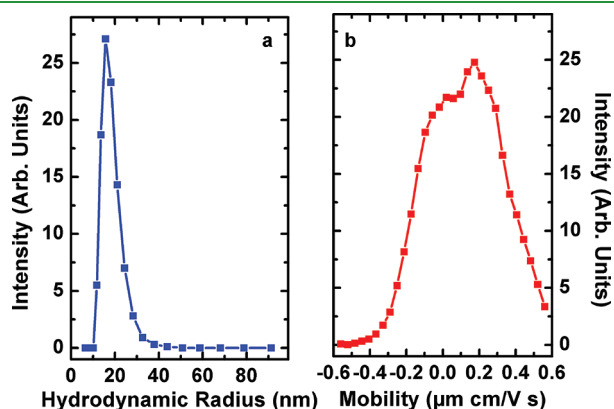


Figure 4. (a) Hydrodynamic diameter distribution of NPs in the EPD suspension. The average diameter is $17 \text{ nm} \pm 3 \text{ nm}$. (b) Electrophoretic mobility of our EPD suspension. The distribution of charged NPs is nearly uniform.

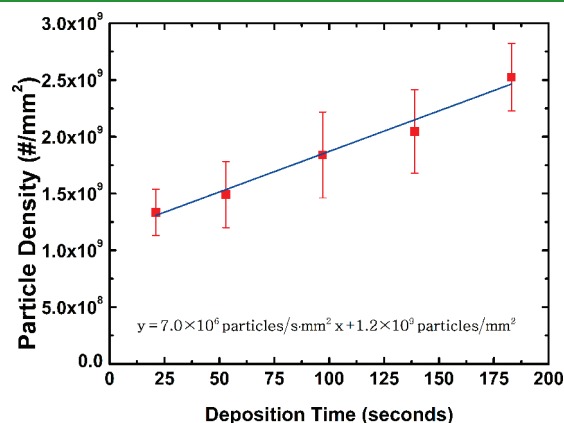


Figure 5. Particle density versus time for monolayer deposition, the slope of the line gives particle flux. A linear result is consistent with deposition at a constant voltage.

and dynamic light scattering measurements of particles size remained constant before and after EPD, we assume that all particles that reached the electrode also deposited. This could explain the large particle flux at the beginning of the deposition. Nanoparticles that subsequently deposited after this initial 30 s arrived in the electrode gap region could have originated from a number of sources, for example the diffusion of charged nanoparticles from the EPD suspension outside of the electrodes into the gap region or the deposition of nanoparticles with notably weaker mobility than those that initially deposited.^{41–44}

With the basis of monolayer formation addressed, we shift our attention to multilayer film formation, as depicted in Figure 6. For these experiments, the NP deposition rate was markedly larger ($1.0 \times 10^9 \pm 7 \times 10^8 \text{ particles/s mm}^2$) than that for the monolayer film because of an increased concentration of charged nanoparticles. Figure 6a shows deposition after 10 s; cluster formation and chain growth to create a network were clearly visible. In Figure 6b, 32 s of deposition are shown, in which the network incorporated nearly every NP. In Figure 6c, new behavior emerged after 64 s of deposition. With the voids nearly filled, NPs began depositing on top of the initial monolayer, forming a bilayer. NPs that formed the bilayer were distinguishable from those in the monolayer under SEM, as they are brighter than the underlying monolayer nanoparticles because of charging effects during SEM imaging.

We observed continued bilayer growth in Figure 6d, a region that constituted 100s of NP deposition. Cluster growth occurred in the bilayer; however, the formation of those bilayer clusters did not exactly mirror the growth of the underlying monolayer. Networking among the clusters was not nearly as extensive. Voids in the underlying monolayer appear to have prevented the bilayer from evolving into a completely filled layer, as the edges of many bilayer regions corresponded to the edges of voids in the underlying monolayer. This suppressed the growth of NP chains that facilitated the networking of NPs, as was observed in the monolayer images. Figure 6e represents the deposited film after 130s and displays hexagonally packed clusters in the nearly complete overlying bilayer. Voids in the first monolayer, which stunted the development of the bilayer, are readily apparent on the right side of the image.

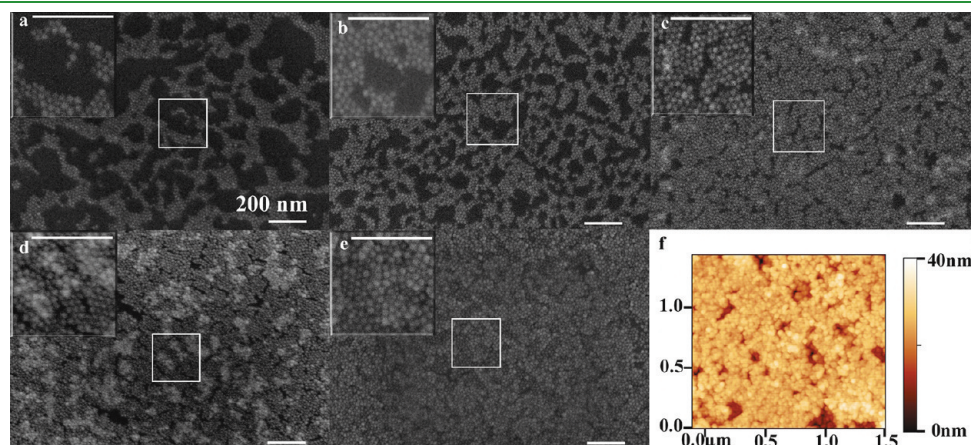


Figure 6. Chronology showing growth of multilayer film. (a) Initial growth of monolayer. (b) Clusters began to network within the monolayer. (c) Monolayer growth nearly completed and bilayer (brighter regions) growth had begun. (d) Bilayer particles packed hexagonally, voids in the underlying monolayer appear to have inhibited the network of the bilayer. (e) Bilayer growth appeared to have been suppressed by larger voids in underlying monolayer. (f) AFM image of the same region of film depicted in e. The bilayer appeared to be nearly complete. The first NPs of the trilayer had deposited onto the film. Collectively, these images support a monolayer-by-monolayer film formation process. (Scale bar and inset scale bar for images a–e = 200 nm; solution concentration, $\sim 1 \text{ mg/mL}$).

Figure 6f shows an atomic force micrograph of the film after 130s of deposition. Highlighted in this image are the exposed, underlying monolayer a nearly complete bilayer and the very beginning of a trilayer. Line profiles of the image indicated that the step height is one particle diameter from the monolayer to bilayer and bilayer to trilayer. Interestingly, the trilayer did not appear to form until the underlying bilayer had nearly completed, as was observed for the bilayer-atop-monolayer formation. This leads additional credence to the assertion that the film formation for these iron oxide nanoparticles followed a monolayer-by-monolayer growth process.

CONCLUSIONS

We have fabricated monolayer films of wüstite/magnetite core/shell nanoparticles using electrophoretic deposition. By varying the concentration of charged nanoparticles within the solution and by controlling the time of the EPD, we controlled both the rate of deposition and the total nanoparticle density in the film. Nearly complete monolayer and multilayer films were produced that illustrated tightly packed, hexagonal arrangements among the NPs, strongly suggestive of possible magnetic interactions (dipole–dipole) among the NPs. The calculated deposition rates and the electrophoretic mobility measurements provide support for a possible explanation behind the production of multilayer films, given the consumption and depletion of charged nanoparticles between the parallel plate electrodes. Evidence of ordered monolayer films and the ease of creating multilayers based on said monolayers provide substantial promise for future device applications, ones for which the facile assembly of macroscopic, tightly packed, ordered casts of nanoparticles, i.e., a crystal of nanocrystals, could be transformative.

ASSOCIATED CONTENT

S Supporting Information. S.1 Calculations for particle–particle spacing and error. S.2 Mobility measurements before and after EPD. This material is available free of charge via the Internet at <http://pubs.acs.org/>.

AUTHOR INFORMATION

Corresponding Author

*E-mail: james.dickerson@vanderbilt.edu.

ACKNOWLEDGMENT

The authors thank Susan Sutton and Tennessee State University for SEM and AFM use. This research is partially supported by the United States Office of Naval Research, Award N000140910523, the National Science Foundation (NSF), Award DMR-0757380, and Award DMR-1054161.

REFERENCES

- (1) Talapin, D. V.; Lee, J. S.; Kovalenko, M. V.; Shevchenko, E. V. *Chem. Rev.* **2010**, *110*, 389–458.
- (2) Freeman, R. G.; Grabar, K. C.; Allison, K. J.; Bright, R. M.; Davis, J. A.; Guthrie, A. P.; Hommer, M. B.; Jackson, M. A.; Smith, P. C.; Walter, D. G.; Natan, M. J. *Science* **1995**, *267*, 1629–1632.
- (3) Okamoto, T.; Yamaguchi, I.; Kobayashi, T. *Opt. Lett.* **2000**, *25*, 372–374.
- (4) Maier, S. A.; Kik, P. G.; Atwater, H. A.; Meltzer, S.; Harel, E.; Koel, B. E.; Requicha, A. A. G. *Nat. Mater.* **2003**, *2*, 229–232.
- (5) Ahnizay, A.; Sakamoto, Y.; Bergstrom, L. *Proc. Natl. Acad. Sci. U.S.A.* **2007**, *104*, 17570–17574.
- (6) Bao, Y. P.; Beerman, M.; Krishnan, K. M. *J. Magn. Magn. Mater.* **2004**, *272*, E1367–E1368.

- (7) Jiang, C. Y.; Tsukruk, V. V. *Adv. Mater.* **2006**, *18*, 829–840.
- (8) Kim, F.; Kwan, S.; Akana, J.; Yang, P. D. *J. Am. Chem. Soc.* **2001**, *123*, 4360–4361.
- (9) Lin, X. M.; Jaeger, H. M.; Sorensen, C. M.; Klabunde, K. J. *J. Phys. Chem. B* **2001**, *105*, 3353–3357.
- (10) Salzemann, C.; Richardi, J.; Lisiecki, I.; Weis, J. J.; Pileni, M. P. *Phys. Rev. Lett.* **2009**, *102*.
- (11) Shevchenko, E. V.; Talapin, D. V.; Kotov, N. A.; O'Brien, S.; Murray, C. B. *Nature* **2006**, *439*, 55–59.
- (12) Talapin, D. V.; Shevchenko, E. V.; Murray, C. B.; Titov, A. V.; Kral, P. *Nano Lett.* **2007**, *7*, 1213–1219.
- (13) Thomas, P. J.; Kulkarni, G. U.; Rao, C. N. R. *J. Phys. Chem. B* **2000**, *104*, 8138–8144.
- (14) Trindade, T.; O'Brien, P.; Pickett, N. L. *Chem. Mater.* **2001**, *13*, 3843–3858.
- (15) Giersig, M.; Mulvaney, P. *Langmuir* **1993**, *9*, 3408–3413.
- (16) Islam, M. A.; Herman, I. P. *Appl. Phys. Lett.* **2002**, *80*, 3823–3825.
- (17) Islam, M. A.; Xia, Y. Q.; Steigerwald, M. L.; Yin, M.; Liu, Z.; O'Brien, S.; Levicky, R.; Herman, I. P. *Nano Lett.* **2003**, *3*, 1603–1606.
- (18) Wong, E. M.; Searson, P. C. *Chem. Mater.* **1999**, *11*, 1959–+.
- (19) Wong, E. M.; Searson, P. C. *Appl. Phys. Lett.* **1999**, *74*, 2939–2941.
- (20) Sarkar, P.; Nicholson, P. S. *J. Am. Ceram. Soc.* **1996**, *79*, 1987–2002.
- (21) Zhitomirsky, I. *Adv. Colloid Interface Sci.* **2002**, *97*, 279–317.
- (22) Hasan, S. A.; Kavich, D. W.; Mahajan, S. V.; Dickerson, J. H. *Thin Solid Films* **2009**, *517*, 2665–2669.
- (23) Hasan, S. A.; Rigueur, J. L.; Harl, R. R.; Krejci, A. J.; Gonzalo-Juan, I.; Rogers, B. R.; Dickerson, J. H. *ACS Nano* **2010**, *4*, 7367–7372.
- (24) Mahajan, S. V.; Cho, J.; Shaffer, M. S. P.; Boccaccini, A. R.; Dickerson, J. H. *J. Eur. Ceram. Soc.* **2010**, *30*, 1145–1150.
- (25) Mahajan, S. V.; Dickerson, J. H. *Nanotechnology* **2010**, *21*.
- (26) Song, M. G.; Bishop, K. J. M.; Pinchuk, A. O.; Kowalczyk, B.; Grzybowski, B. A. *J. Phys. Chem. C* **2010**, *114*, 8800–8805.
- (27) Gonzalez, A.; Ramos, A.; Green, N. G.; Castellanos, A.; Morgan, H. *Phys. Rev. E: Stat., Nonlinear, Soft Matter Phys.* **2000**, *61*, 4019–4028.
- (28) Ryan, K. M.; Mastroianni, A.; Stancil, K. A.; Liu, H. T.; Alivisatos, A. P. *Nano Lett.* **2006**, *6*, 1479–1482.
- (29) Giersig, M.; Mulvaney, P. *J. Phys. Chem.* **1993**, *97*, 6334–6336.
- (30) Teranishi, T.; Hosoe, M.; Miyake, M. *Adv. Mater.* **1997**, *9*, 65.
- (31) Park, J.; An, K. J.; Hwang, Y. S.; Park, J. G.; Noh, H. J.; Kim, J. Y.; Park, J. H.; Hwang, N. M.; Hyeon, T. *Nat. Mater.* **2004**, *3*, 891–895.
- (32) Kovalenko, M. V.; Bodnarchuk, M. I.; Lechner, R. T.; Hesser, G.; Schaffler, F.; Heiss, W. *J. Am. Chem. Soc.* **2007**, *129*, 6352–+.
- (33) Hasan, S. A.; Kavich, D. W.; Dickerson, J. H. *Chem. Commun.* **2009**, 3723–3725.
- (34) Mahajan, S. V.; Kavich, D. W.; Redigolo, M. L.; Dickerson, J. H. *J. Mater. Sci.* **2006**, *41*, 8160–8165.
- (35) Verde, M.; Caballero, A. C.; Iglesias, Y.; Villegas, M.; Ferrari, B. *J. Electrochem. Soc.* **2010**, *157*, H55–H59.
- (36) Gill, V.; Guduru, P. R.; Sheldon, B. W. *Int. J. Solids Struct.* **2008**, *45*, 943–958.
- (37) Golan, S.; Elata, D.; Orenstein, M.; Dinnar, U. *Electrophoresis* **2006**, *27*, 4919–4926.
- (38) Green, N. G.; Ramos, A.; Morgan, H. *J. Electrostatics* **2002**, *56*, 235–254.
- (39) Lee, S.; Zhang, Y. H.; White, H. S.; Harrell, C. C.; Martin, C. R. *Anal. Chem.* **2004**, *76*, 6108–6115.
- (40) Li, W. H.; Du, H.; Chen, D. F.; Shu, C. *Comput. Mater. Sci.* **2004**, *30*, 320–325.
- (41) Besra, L.; Samantaray, P.; Bhattacharjee, S.; Singh, B. P. *J. Mater. Sci.* **2007**, *42*, 5714–5721.
- (42) Ciou, S.-J.; Fung, K.-Z.; Chiang, K.-W. *J. Power Sources* **2007**, *172*, 358–362.
- (43) Wang, Y. C.; Leu, I. C.; Hon, M. H. *J. Am. Ceram. Soc.* **2004**, *87*, 84–88.
- (44) González-Cuenca, M.; Biesheuvel, P. M.; Verweij, H. *AlChE J.* **2000**, *46*, 626–631.